STRUCTURAL BIOLOGY

Inhibition mechanism of NKCC1 involves the carboxyl terminus and long-range conformational coupling

Mitchell A. Moseng[1]†, **Chih-Chia Su**[1]†, **Kerri Rios**[2], **Meng Cui**[3], **Meinan Lyu**[1], **Przemyslaw Glaza**[1], **Philip A. Klenotic**[1], **Eric Delpire**[2], **Edward W. Yu**[1]*

The Na-K-2Cl cotransporter-1 (NKCC1) is an electroneutral Na$^+$-dependent transporter responsible for simultaneously translocating Na$^+$, K$^+$, and Cl$^-$ ions into cells. In human tissue, NKCC1 plays a critical role in regulating cytoplasmic volume, fluid intake, chloride homeostasis, and cell polarity. Here, we report four structures of human NKCC1 (hNKCC1), both in the absence and presence of loop diuretic (bumetanide or furosemide), using single-particle cryo–electron microscopy. These structures allow us to directly observe various novel conformations of the hNKCC1 dimer. They also reveal two drug-binding sites located at the transmembrane and cytosolic carboxyl-terminal domains, respectively. Together, our findings enable us to delineate an inhibition mechanism that involves a coupled movement between the cytosolic and transmembrane domains of hNKCC1.

INTRODUCTION

The Na-K-2Cl cotransporter (NKCC) is a membrane protein whose main function is to facilitate the uptake of Na$^+$, K$^+$, and Cl$^-$ ions into the cell. In humans, there are two isoforms, NKCC1 and NKCC2 (*1*, *2*), belonging to the solute carrier 12 (SLC12) family of transporters. Both NKCC1 and NKCC2 are symporters that mediate the electroneutral transport of Cl$^-$ accompanied by Na$^+$ and/or K$^+$ across the plasma membrane. The stoichiometry of ion transport is 1 Na$^+$:1 K$^+$:2 Cl$^-$ based on combined gradients of [Na$^+$] × [K$^+$] × [Cl$^-$] × [Cl$^-$] (*3*). NKCC2 is strictly found in the thick ascending limb of the loop of Henle and the macula densa of nephrons in the kidney, whereas NKCC1 is broadly expressed throughout the body, including organs such as the brain, lung, and intestine and exocrine systems such as the salivary and sweat glands (*4*). In pathologic settings, there is strong evidence to support that disruption of NKCC1 leads to intestinal and pulmonary obstruction, pancreatic insufficiency, chronic gastrointestinal diseases, lung infections, acute and chronic pain, sensorineural hearing loss (*5–8*), and possibly neurodevelopmental disorders (*9*, *10*).

Loop diuretics such as furosemide (Fu) and bumetanide (Bu) target NKCC2 in the kidney for the treatment of hypertension, edema, congestive heart failure, and chronic kidney disease (*11*). These compounds are also effective inhibitors of NKCC1, which suggests a similar method of inhibition that may extend to this entire class of membrane-bound transporters (*12*, *13*). In the circulation, however, loop diuretics are mostly bound to albumin (*14*, *15*), which may explain why these drugs are less effective in reaching peripheral tissues and inhibiting NKCC1. Regardless of this limitation, Bu has been shown to attenuate the severity of neurodevelopmental disorders such as autism spectrum disorders (*16*, *17*) and Fragile X (*18*). However, the molecular mechanisms underlying drug inhibition of the NKCC cotransporters remain elusive despite decades of clinical use of these drugs.

Recently, a cryo–electron microscopy (cryo-EM) structure of NKCC1 from *Danio rerio* (dNKCC1) was reported, with a transmembrane (TM) domain (TMD) and a cytosolic C-terminal domain (CTD) present (*19*). However, the cytosolic N-terminal domain (NTD) is missing, likely because of its highly flexible nature. Data suggest that the TMD participates in ion translocation, whereas the NTD and CTD regulate transport and trafficking. Molecular dynamics (MD) simulations have revealed how this dNKCC1 cotransporter shuttles Na$^+$, K$^+$, and Cl$^-$ across the membrane (*20*). In 2020, a cryo-EM structure of human NKCC1 (hNKCC1) lacking the entire cytosolic domain was solved (*21*). This structure confirms that the fold of the TMD of hNKCC1 largely resembles that of dNKCC1.

To expand upon the structural and functional properties of the NKCC class of transporters, here, we present four structures of the hNKCC1 cotransporter, both in the absence and presence of a loop diuretic drug (Fu or Bu) using single-particle cryo-EM. Unexpectedly, we identified that hNKCC1 has two distinct inhibitor-binding sites, which are located at the CTD and TMD of the cotransporter, respectively. Inhibitors bound at either site cause major conformational differences when compared to unbound forms of this membrane protein. Combined, our cryo-EM, mutagenesis, and MD simulation findings enable us to delineate a mechanism for drug inhibition where the binding of inhibitor at the CTD and/or TMD arrests the cotransporter into a conformation unfavorable to ion permeation.

RESULTS

Cryo-EM structure of apo-hNKCC1

Cumulative clinical studies over the past 5 years suggest that dysfunction of hNKCC1 causes numerous serious diseases, including neurodevelopmental disorders, dysmorphic facial features, deafness, cystic fibrosis TM conductance regulator–like secretory defects accompanied by mucus accumulation in the lung and intestine, and severe xerostomia and hypotonia (*9*). To understand how hNKCC1 functions at the molecular level, we expressed and purified full-length wild-type hNKCC1 in human embryonic kidney 293 cells to determine its structure, both alone and in complex with Bu or Fu, using single-particle cryo-EM.

Three-dimensional (3D) reconstitution of the apo-hNKCC1 cotransporter led to a cryo-EM map that enabled us to solve the structure

[1]Department of Pharmacology, Case Western Reserve University School of Medicine, Cleveland, OH 44106, USA. [2]Department of Anesthesiology, Vanderbilt University School of Medicine, Nashville, TN 37232, USA. [3]Department of Pharmaceutical Sciences, Northeastern University School of Pharmacy, Boston, MA 02115, USA.
*Corresponding author. Email: edward.w.yu@case.edu
†These authors contributed equally to this work.

of this membrane protein. Of the 1211 amino acids per molecule, we included 923 residues (288 to 1210) in our final model (Fig. 1, figs. S1 and S2, and table S1). The TM helices at the TMD and α helices (αs) and β strands (βs) at the CTD of hNKCC1 (fig. S3) are designated numerically from the N to C termini: TM1 (288 to 314), TM2 (317 to 340), TM3 (362 to 396), TM4 (405 to 425), TM5 (331 to 454), TM6 (486 to 508), TM7 (518 to 543), TM8 (600 to 632), TM9 (652 to 667), TM10 (671 to 698), TM11 (713 to 729), TM12 (732 to 752), α0 (764 to 779), β1 (787 to 794), α1 (798 to 811), β2 (817 to 821), α2 (832 to 848), β3 (852 to 859), α3 (863 to 872), β4 (882 to 887), α4 (901 to 912), β5 (916 to 921), α5 (1009 to 1018), β6 (1023 to 1028), α6 (1031 to 1043), β7 (1053 to 1060), α7 (1062 to 1079), β8 (1085 to 1091), α8 (1099 to 1111), α9 (1120 to 1127), α10 (1136 to 1149), β9 (1158 to 1169), α11 (1175 to 1189), and β9 (1192 to 1201).

Similar to the structure of dNKCC1 (19), the apo-hNKCC1 membrane protein presents a dimeric oligomerization with a pseudo two-fold symmetry axis perpendicular to the membrane surface (Fig. 1, A and B). Each subunit of hNKCC1 has 12 TM helices that constitutes the TMD, where TM helices TM1 to TM5 and TM6 to TM10 create an inverted repeat architecture (fig. S3). TM11 and TM12, combined with the C-terminal end of TM10, form the dimer interface. TM11 and TM12 are relatively short in comparison with the other TM helices. Globally, the hNKCC1 dimer features a concave aqueous basin facing the extracellular side (Fig. 1B). This basin presumably allows the aqueous solution to reach the midpoint of the membrane bilayer.

The hNKCC1 protomer also has a relatively small extracellular domain formed by extracellular loops connecting consecutive TM helices (Fig. 1B). Particularly, the extracellular loops between TM5 and TM6 (EL3) and between TM7 and TM8 (EL4) contribute most of the structural elements of the extracellular domain (fig. S3). It has been suggested that this domain is critical for surface expression and transport regulation (19).

The cytosolic CTD of each hNKCC1 molecule consists of 11 α helices and 10 β strands that form a large 430–amino acid structural domain (fig. S3). This CTD is actively engaged in transport activation, and dimerization of this domain plays a role in the regulatory mechanism (19). The CTD is connected with the TMD via a flexible linker consisting of approximately 23 residues (residues 760 to 782). Residues 764 to 778 also form an α-helical linker helix (α0). Consistent with the dimeric dNKCC1 structure (19), this elongated linker extends the secondary structural elements of one subunit of hNKCC1 across the dimer interface, bringing the CTD crossover to the next hNKCC1 subunit and creating a scissor-like architecture. In general, the secondary structure of the CTD of hNKCC1 is in agreement with that of dNKCC1. However, a detailed inspection reveals discrepancies between the two. For example, the fold of residues 1120 to 1130 of hNKCC1 is quite distinct from the corresponding residues of dNKCC1 (fig. S4). Notably, the overall structure of the CTD in this family of transporters is well conserved, as the CTD of Na^+-independent KCC cotransporters follow a very similar architecture (22, 23). As with the cryo-EM structure of dNKCC1 (19), we did not observe cryo-EM densities arising from the NTD of hNKCC1, indicating that this domain is highly flexible.

hNKCC1 cotransports Na^+, K^+, and Cl^- ions in a molar ratio of 1:1:2. In the TMD of each protomer of the transporter, we identified two spherical-shaped extra densities corresponding to bound K^+ and Cl^- ions (Fig. 1B). These two ions are found to associate with each other. Unfortunately, we did not observe extra densities correlating to Na^+ and the second Cl^- ion. Within 3.0 Å of bound K^+, the side-chain oxygen of Y383 is directly involved in anchoring this positively charged ion. In addition, the backbone oxygens of N298, I299, P496, and T499 strongly coordinate with this K^+. The bound Cl^- also interacts with K^+, forming the sixth coordination site for this positively charged ion (Fig. 1B). This feature is also conserved in KCC cotransporters (22, 23). In agreement with the structure of dNKCC1, our cryo-EM structure reveals that apo-hNKCC1 is captured in an inward-open conformation (Fig. 1C).

Cryo-EM structures of the hNKCC1-Fu complex

To elucidate the molecular mechanism of drug inhibition, we determined a cryo-EM structure of hNKCC1 in the presence of the inhibitor Fu. We recently developed a "Build and Retrieve" (BaR) cryo-EM methodology (24) capable of performing in silico purification and sorting of images from a large heterogeneous dataset. BaR allows us to sort images into several different classes of proteins and/or
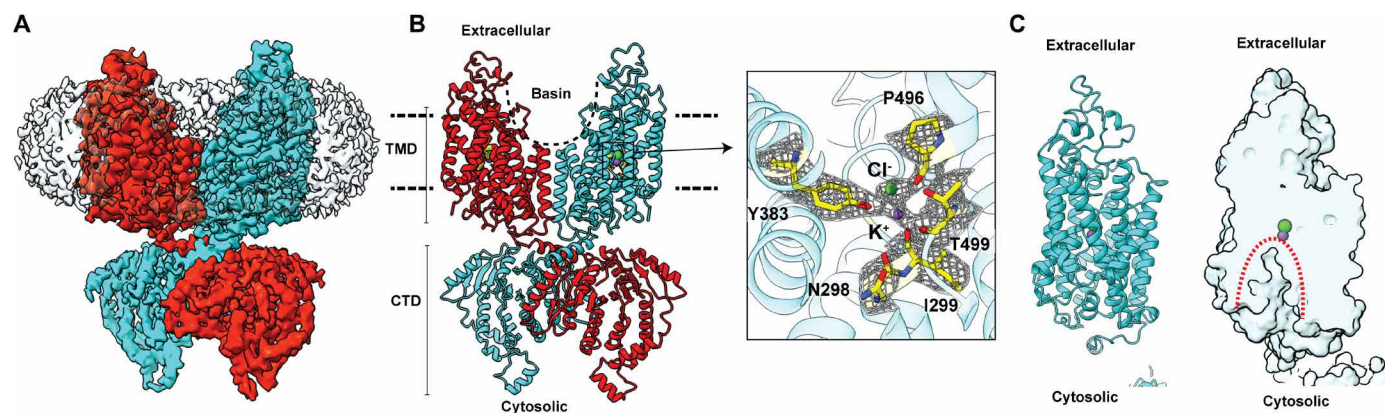

Fig. 1. Structure of apo-hNKCC1. (A) Side view of the cryo-EM map of the apo-hNKCC1 dimer viewed in the membrane plane. The hNKCC1 protomers are colored cyan and red. The detergent micelles surrounding the TMD of hNKCC1 are highlighted with gray color. **(B)** Ribbon diagram of the apo-hNKCC1 dimer viewed in the membrane plane. The hNKCC1 protomers are colored cyan and red. Each hNKCC1 protomer contains one bound K^+ (purple sphere) and one bound Cl^- (green sphere). Residues coordinating with these ions are in yellow sticks. The local cryo-EM densities of bound K^+ and Cl^- are in gray meshes. **(C)** Surface representation of apo-hNKCC1. This figure reveals that the structure of apo-hNKCC1 is captured in an inward-open conformation.

different conformations of a singular protein. Extensive classification of the single-particle images using BaR indicated that there were two distinct populations of hNKCC1 with unique conformations coexisting in our sample (figs. S5 and S6 and table S1). Similar to apo-hNKCC1, the two hNKCC1-Fu complexes (hNKCC1-Fu-I and hNKCC1-Fu-II) assemble as dimers (Figs. 2 and 3). However, no cryo-EM densities corresponding to bound ions were found in the structures of either hNKCC1-Fu-I or hNKCC1-Fu-II (fig. S7).

Structure of hNKCC1-Fu-I
Overall, the conformation of the cryo-EM structure of hNKCC1-Fu-I is comparable to that of apo-hNKCC1 (Fig. 2, A and B). However, there are some notable conformational differences between these two structures. Superimposition of these two structural models gives rise to a root mean square deviation (RMSD) of 1.1 Å (Fig. 2C). The conformation of hNKCC1-Fu-I is distinct in that the CTD of the dimer bends toward the membrane surface by 9 Å when compared to the CTD of apo-hNKCC1. This shift in location can be explained

as a rigid body movement of the CTD with respect to the TMD. This change is, in part, due to an 8° rotational motion at the C terminus of the linker helix between these two domains (Fig. 2C). This movement leads to a shift of the C-terminal end of this linker helix, positioning it 4 Å closer to the membrane plane. The conformational change may also be related to a subtle alteration of the hydrogen bond rearrangement of the dimer interface at the cytoplasmic surface of the membrane. In apo-hNKCC1, the conserved residues H695 of TM10 and Y751′ of TM12 (where the prime is used to designate residues from the next protomer) interact to form a hydrogen bond. These two residues shift apart and break this hydrogen bond in the hNKCC1-Fu-I structure (Fig. 2C). This movement, in turn, helps reorient the flexible CTD to a new position in the hNKCC1-Fu-I structure. On the basis of the structural information, hNKCC1-Fu-I is trapped in an occluded conformation (Fig. 2D).

An extra density compatible with Fu (Fig. 2B and fig. S5) was found within a pocket formed by each hNKCC1 protomer located
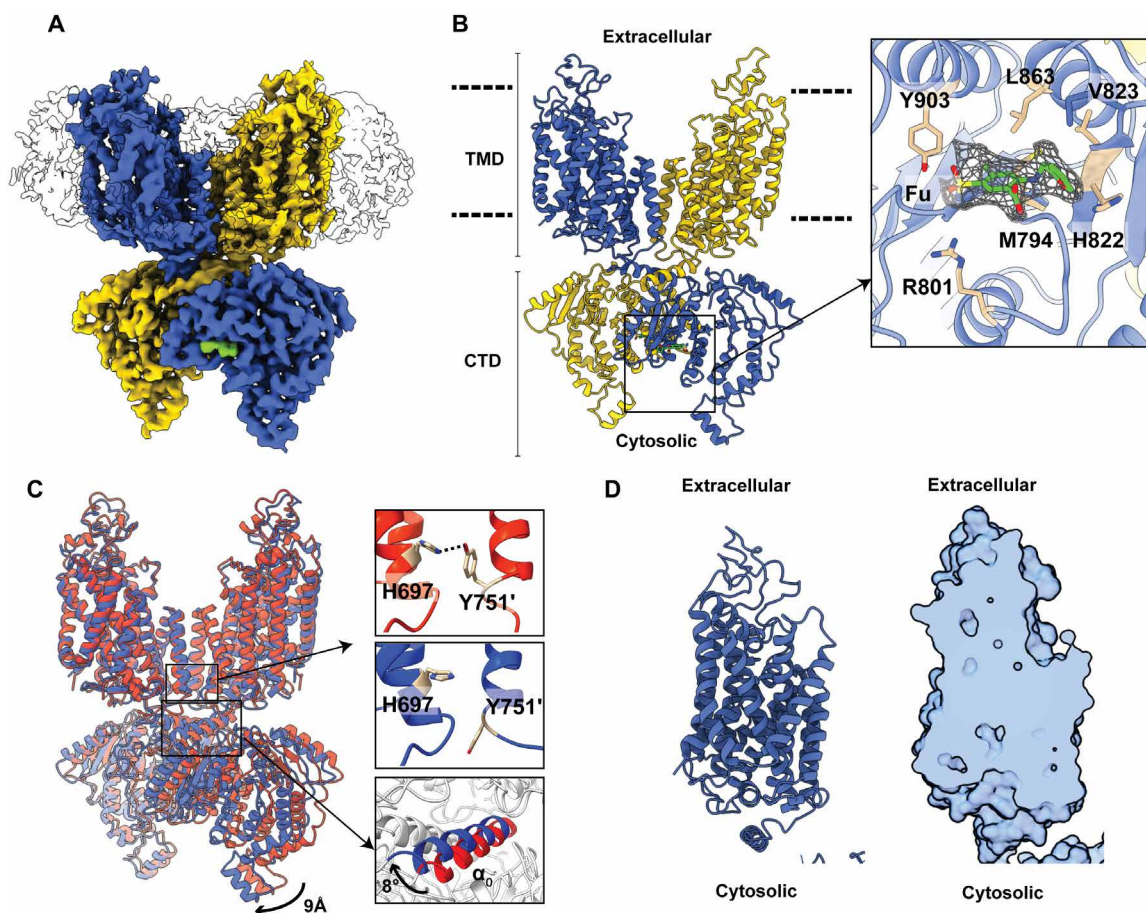

Fig. 2. Structure of hNKCC1-Fu-I. (**A**) Side view of the cryo-EM map and ribbon diagram of the hNKCC1-Fu-I dimer viewed in the membrane plane. The hNKCC1 protomers are colored yellow and blue. The detergent micelles surrounding the TMD of hNKCC1 are highlighted with gray color. Each hNKCC1 protomer is found to bind a Fu molecule (colored green). (**B**) Ribbon diagram of the hNKCC1-Fu-I dimer viewed in the membrane plane. The hNKCC1 protomers are colored yellow and blue. The bound Fu molecule in the cotransporter is represented by green sticks. Density of bound Fu is in gray meshes. Residues involved in binding Fu are in wheat sticks. (**C**) Superimposition of the structures of apo-hNKCC1 and hNKCC1-Fu-I. The apo-hNKCC1 and hNKCC1-Fu-I structures are colored red and blue, respectively. This superimposition suggests that the entire CTD of hNKCC1-Fu-I is able to bend toward the membrane surface by 9 Å in comparison with that of apo-hNKCC1. This conformational change is accompanied by an 8° rotational motion at the C terminus of the linker helix (α0) (red, apo-hNKCC1; blue, hNKCC1-Fu-I) and the breaking of a hydrogen bond between residues H695 and Y751′ (red, apo-hNKCC1; blue, hNKCC1-Fu-I). (**D**) Surface representation of hNKCC1-Fu-I. This figure reveals that the structure of hNKCC1-Fu-I is captured in an occluded conformation.
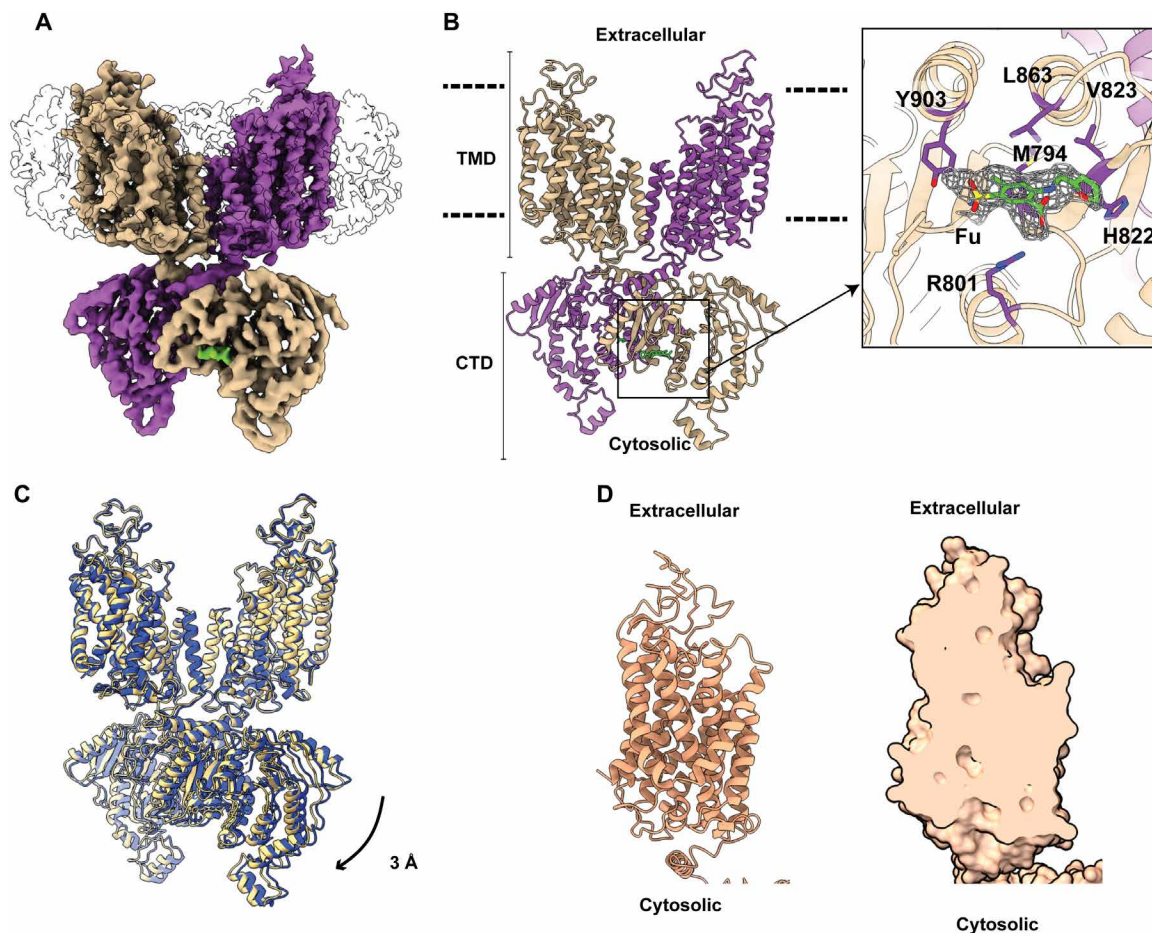
Fig. 3. Structure of hNKCC1-Fu-II. (**A**) Side view of the cryo-EM map and ribbon diagram of the hNKCC1-Fu-II dimer viewed in the membrane plane. The hNKCC1 protomers are colored purple and light brown. The detergent belt of the dimer is highlighted with gray color. Each hNKCC1 protomer is found to bind a Fu molecule (colored green). (**B**) Ribbon diagram of the hNKCC1-Fu-II dimer viewed in the membrane plane. The hNKCC1 protomers are colored purple and light brown. The bound Fu molecule in the cotransporter is represented by green sticks. Density of bound Fu is in gray meshes. Residues involved in binding Fu are in purple sticks. (**C**) Superimposition of the structures of hNKCC1-Fu-I and hNKCC1-Fu-II. The hNKCC1-Fu-I and hNKCC1-Fu-II structures are colored blue and yellow, respectively. This superimposition suggests that the entire CTD of hNKCC1-Fu-II further bends toward the membrane surface by another 3 Å in comparison with that of hNKCC1-Fu-I. (**D**) Surface representation of hNKCC1-Fu-II. This figure reveals that the structure of hNKCC1-Fu-II is captured in an occluded conformation.

at the outermost surface of the CTD of hNKCC1-Fu-I. The shape of this extra density suggests that this pocket is capable of binding this compound. The bound Fu is surrounded by six residues: M794, R801, H822, V823, L863, and Y903. Notably, our mutagenesis experiments indicate that mutations of R801, H822, and Y903 markedly reduce the inhibitory effect of this diuretic (see below), suggesting that these residues are critical for Fu binding to hNKCC1.

Structure of hNKCC1-Fu-II

Our data suggests that the conformation of the hNKCC1 dimer in the hNKCC1-Fu-II structure depicts a unique conformational state (Fig. 3, A and B). Pairwise superimpositions of the hNKCC1-Fu-II dimer onto those of apo-hNKCC1 and hNKCC1-Fu-I give rise to RMSD values of 1.3 and 1.1 Å. A closer inspection of the hNKCC1-Fu-II structure suggests that there is a change in conformation of the CTD in comparison with those of apo-hNKCC1 and hNKCC1-Fu-I. This change can be interpreted as a rigid-body rotation of the entire CTD toward the membrane plane with respect to the TMD. This rigid-body motion accompanies the shift in position of the CTD, leading this domain to further bend toward the surface of

the cytoplasmic membrane by an additional 3 Å when compared with that of the hNKCC1-Fu-I structure (Fig. 3C). The structures of apo-hNKCC1, hNKCC1-Fu-I, and hNKCC1-Fu-II can be interpreted as snapshots of different conformations of the cotransporter that highlight a shift in position of the CTD (Figs. 2C and 3C). As with hNKCC1-Fu-I, the structure of hNKCC1-Fu-II is caught in an occluded conformation (Fig. 3D).

Similar to the hNKCC1-Fu-I structure, the Fu inhibitor is found to bind at the identical drug-binding site, with M794, R801, H822, V823, L863, and Y903 responsible for the binding (Fig. 3B and fig. S5). It appears that binding of Fu at the CTD triggers a shift in position of the CTD in relation to the TMD in both structures of hNKCC1-Fu-I and hNKCC1-Fu-II.

Cryo-EM structures of the hNKCC1-Bu complex

In hopes of determining a second hNKCC1-inhibitor bound structure, we incubated the hNKCC1 protein with Bu. The single-particle images collected allowed us to solve the structure of the hNKCC1-Bu complex (figs. S8 and S9 and table S1). Notably, the structure of

hNKCC1-Bu is very distinct from those of apo-hNKCC1, hNKCC1-Fu-I, and hNKCC1-Fu-II. The organization of the hNKCC1 dimer is packed in a way that can be interpreted as two independent monomers within the TM region, where the two TMDs are significantly distant from each other and do not appear to participate in intersubunit interactions (Fig. 4, A and B). This is expected, as the architecture of hNKCC1 features a concave aqueous basin that likely allows for water to reach the midpoint of the membrane bilayer at the interface of the hNKCC1 dimer (Fig. 1B). TM11 and TM12 of

each protomer are responsible for creating the dimerization interface (Fig. 4B). These two helices are significantly shorter, which substantially decreases the area of the dimer interface between the two protomers. TM11 and TM12 form a V-shaped feature to link each protomer at the midpoint of the membrane bilayer. The distance between the tips of the two V-shaped features within the apo-hNKCC1, hNKCC1-Fu-I, and hNKCC1-Fu-II dimers, as measured between the Cα atoms of W732 and W732′, range from 7.1 to 10.6 Å. However, this distance becomes 27.5 Å in the hNKCC1-Bu structure (Fig. 4C),
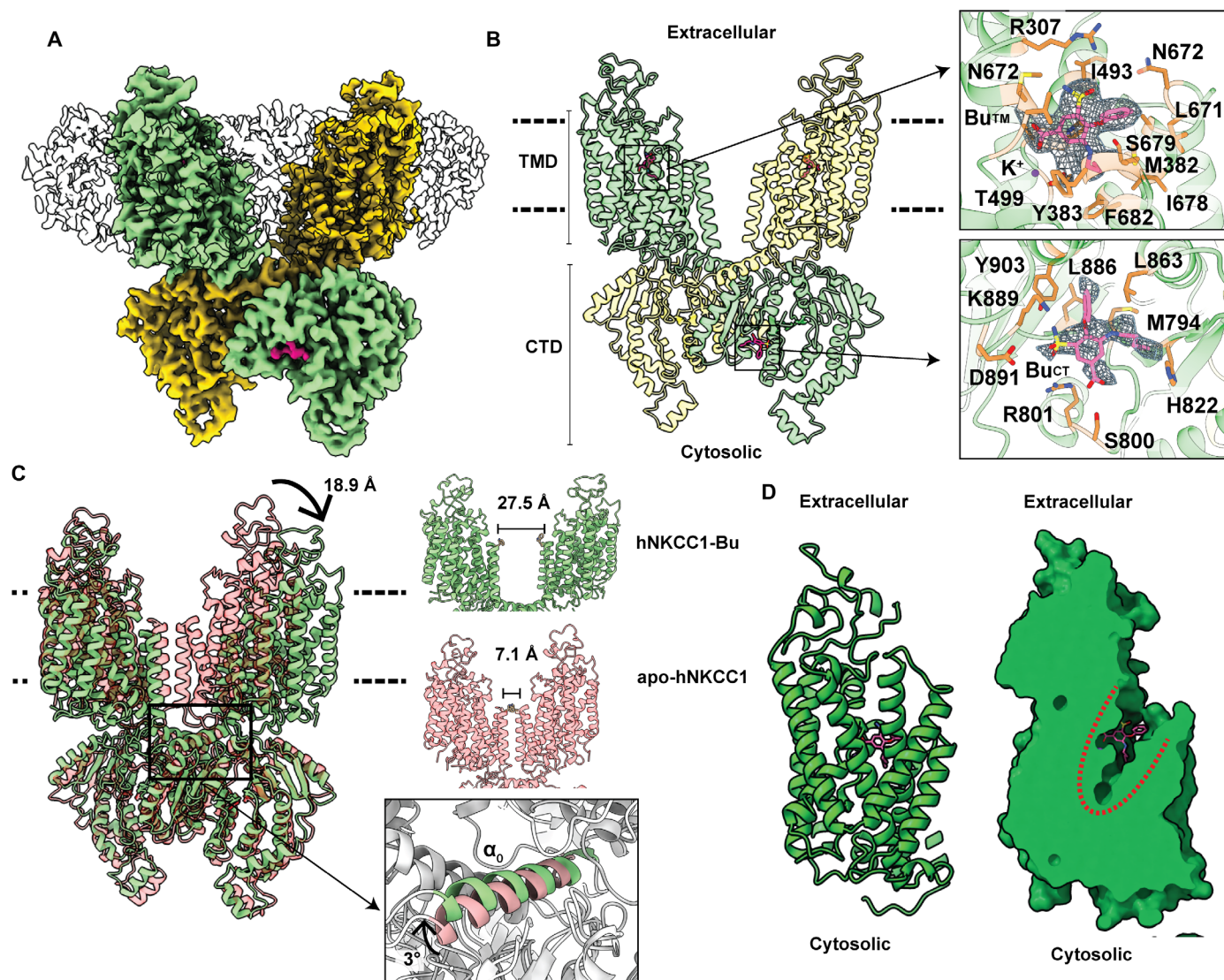

Fig. 4. Structure of hNKCC1-Bu. (**A**) Side view of the cryo-EM map and ribbon diagram of the hNKCC1-Bu dimer viewed in the membrane plane. The hNKCC1 protomers are colored yellow and green. The detergent micelles surrounding the TMD of hNKCC1-Bu are highlighted with gray color. The bound Bu molecules at the CTD and TMD are in magenta. (**B**) Ribbon diagram of the hNKCC1-Bu dimer viewed in the membrane plane. The hNKCC1 protomers are colored yellow and green. The bound Bu$_{CT}$ and Bu$_{TM}$ molecules are in gray meshes. Residues involved in binding these two Bu molecules are in orange sticks. Residues M794, S800, R801, H822, L863, L886, D891, K889, and Y903 are engaged in anchoring Bu$_{CT}$ at the CTD, whereas residues R307, M382, Y383, I493, T499, L671, N672, I678, S679, and S682 participate in contacting Bu$_{TM}$ at the TMD. (**C**) Superimposition of apo-hNKCC1 and hNKCC1-Bu. The apo-hNKCC1 and hNKCC1-Bu structures are colored pink and green, respectively. This superimposition suggests that the configuration of the TMD of hNKCC1 shifts from a dimeric assembly to two independent monomers. The tip-to-tip distance, as measured between Cα atoms of W732 and W732′, shifts from 7.1 Å (for apo-hNKCC1) to 27.5 Å (for hNKCC1-Bu). This change is accompanied by a 3° rotation and 6 Å shift of the linker helix (α0) (pink, apo-hNKCC1; green, hNKCC1-Bu) toward the TMD when compared with the structures of hNKCC1-Bu and apo-hNKCC1. It also associates with a rigid-body movement of a TMD of one hNKCC1 subunit in relation to its CTD, leading to an overall 18.9 Å shift in location of its EL4 extracellular loop. (**D**) Surface representation of hNKCC1-Bu. This figure reveals that the structure of hNKCC1-Bu is captured in an outward-open conformation.

which is 17 to 20 Å greater than those of apo-hNKCC1, hNKCC1-Fu-I, and hNKCC1-Fu-II. It appears that the presence of Bu triggers a significant conformational change such that the hNKCC1 dimer separates into two monomers at the TM region. In comparison with the structures of apo-hNKCC1 and hNKCC1-Bu, this change in conformation can be interpreted as a rigid-body movement of the TMD of one subunit with respect to that of the other subunit, leading to an overall 18.9 Å shift in location of its EL4 extracellular loop (Fig. 4C). However, the two protomers of hNKCC1-Bu still have specific contact via their CTDs to maintain a dimeric organization (Fig. 4, A and B).

As in the structures of hNKCC1-Fu-I and hNKCC1-Fu-II, we observed an extra density located at the putative drug-binding site of the CTD, indicating the existence of a bound Bu inhibitor in the cryo-EM structure of hNKCC1-Bu. Residues M794, S800, R801, H822, L863, L886, D891, K889, and Y903 are engaged in anchoring this Bu inhibitor (Fig. 4B). This Bu binding site overlaps with that of Fu.

Different from the structures of hNKCC1-Fu-I and hNKCC1-Fu-II, we identified an additional bound Bu molecule located at the TMD of the hNKCC1-Bu complex. A cavity formed among TMs 1, 3, 6, 8, 9, and 10, facing the extracellular space, creates this Bu binding site. Specifically, residues R307, M382, Y383, I493, T499, L671, N672, I678, S679, and S682 are responsible for anchoring this inhibitor (Fig. 4B). A K^+ ion was also found in the vicinity of bound Bu. Apparently, the benzoate acidic group of this loop diuretic directly contacts the K^+ ion, securing the binding. Comparing the structure of apo-hNKCC1 with that of hNKCC1-Bu, it is interesting to note that the bound Cl^- ion (in apo-hNKCC1) is found to be replaced by bound Bu (in hNKCC1-Bu) for interacting with the bound K^+ ion. Given that hNKCC1 contains two Bu binding sites, we therefore designated these sites at the CTD and TMD as Bu_{CT} and Bu_{TM}, respectively. Unexpectedly, our cryo-EM data depicts that the structure of hNKCC1-Bu represents an outward-open conformational state (Fig. 4D).

K+ influx measurements in *Xenopus laevis* oocytes encoding mouse NKCC1

On the basis of extensive kinetic and mutagenesis studies (*25–28*), it is evidenced that diuretic drugs bind within the permeation pathway for ions at the TMD of NKCC1. This location should correspond to the Bu_{TM} binding site at the TMD. Unexpectedly, our cryo-EM data also suggest a possibility of anchoring these inhibitors at the CTD of the cotransporter (Fu and Bu_{CT} sites) (Fig. 5A). To assess the role of these substrate-binding pockets within the CTD for drug inhibition, we performed mutagenesis of homologous residues in mouse NKCC1 (mNKCC1) and tested their function in *X. laevis* oocytes. Overall, the hNKCC1 and mNKCC1 cotransporters share 95.5% homology and 93.9% identity at the amino acid level. The greatest divergence of these two proteins occurs at the N termini, whereas their C termini have higher conservation with 97.6% homology and 95.9% identity in protein sequences (fig. S10). Residues R795, H816, and Y897 of mNKCC1 (corresponding to R801, H822, and Y903 in hNKCC1) were mutated into alanine residues (Fig. 5, B and C), as these three residues in hNKCC1 coordinate with both Fu and Bu in the cryo-EM structures. We found that mutation of R795 (R801), although reducing transporter function by itself, also showed decreased sensitivity to Bu (Fig. 5C). When these inhibitors were tested at 400 nM, a concentration that is close to the transporter median effective concentration (EC$_{50}$), inhibition was reduced from 50 to 8 to 10%. This

effect was similar (13% inhibition) when the R795A/H816A (R801/H822A) double mutant was tested (Fig. 5C). With the R795A/Y897A (R801A/Y903A) double mutant, 400 nM Bu completely failed to affect mNKCC1 (0% inhibition, Fig. 5C). At the higher dose of 10 µM, the difference was less pronounced, as Fu inhibited the R795A (R801A) mutant by only 40%, compared to 56% with control NKCC1 (Fig. 5B) with the other two single-point mutations showing no effect.

Computational simulations of the hNKCC1 cotransporter

We performed MD simulations on the basis of our cryo-EM structure of apo-hNKCC1. The root mean square fluctuation (RMSF) of Cα atoms (based on the 1000-ns simulation trajectory) indicates that there are four flexible regions of the cotransporter (fig. S11), with two found in the CTD and the other two located at the TMD. Principle components analysis (PCA) suggests that the first two eigenvectors account for 58% of the global motion of the hNKCC1 cotransporter (fig. S12). The first eigenvector, which depicts the most important motions extracted from MD simulation trajectories, corresponds to the rigid-body rotational motions of both the CTD and TMD (fig. S13). The second eigenvector represents the rigid-body rotational motion of the CTD (fig. S13). These calculated results agree with our cryo-EM structures, suggesting that the major conformational difference among these structures is the relative locations of the CTD and TMD.

DISCUSSION

In this study, we successfully resolved cryo-EM structures of the hNKCC1 cotransporter, both in the absence and presence of the diuretic drugs Fu or Bu. These structures allowed us to directly observe various conformations of hNKCC1, providing important insight into the mechanism of drug inhibition.

One major difference between the structures of apo-hNKCC1, hNKCC1-Fu-I, and hNKCC1-Fu-II is the conformation of the CTD. This domain is able to perform a rigid-body rotational motion with respect to the TMD, allowing for the cotransporter to alter its conformation (Figs. 2C and 3C). In contrast, upon analysis of the apo-hNKCC1 and hNKCC1-Bu structures, it appears that the assembly of the TMD is capable of switching from dimeric to monomeric oligomerizations (Fig. 4C). It is possible that these two major movements couple together to facilitate the transition of hNKCC1 to various conformational states. Our MD calculations show that the major functional dynamics of this cotransporter correspond to the rigid-body rotational motions of both the CTD and TMD. The movement of the TMD within the hNKCC1 dimer is able to disengage the dimeric assembly of the two TMDs of hNKCC1 protomers and break them into two independent, monomeric TMDs. Therefore, the TM region of hNKCC1 can either form a dimeric assembly or dissociate into two independent monomeric units (Figs. 1 to 4). The transition of conformations at the CTD and TMD may couple together to inhibit its transport function. These changes likely cause a long-distance coupling interaction, leading the cotransporter to shift its conformation from inward-open to occluded and outward-open states. These changes in conformation, in turn, prohibit the shuttling of ions.

The phenomenon of switching between different oligomeric states of the TMD within a transporter has been observed in the *Acinetobacter baumannii* (*Acinetobacter* drug efflux B) multidrug efflux pump, where this trimeric AdeB membrane protein can be assembled as a "trimer," "dimer + monomer", or "monomer + monomer + monomer" at the
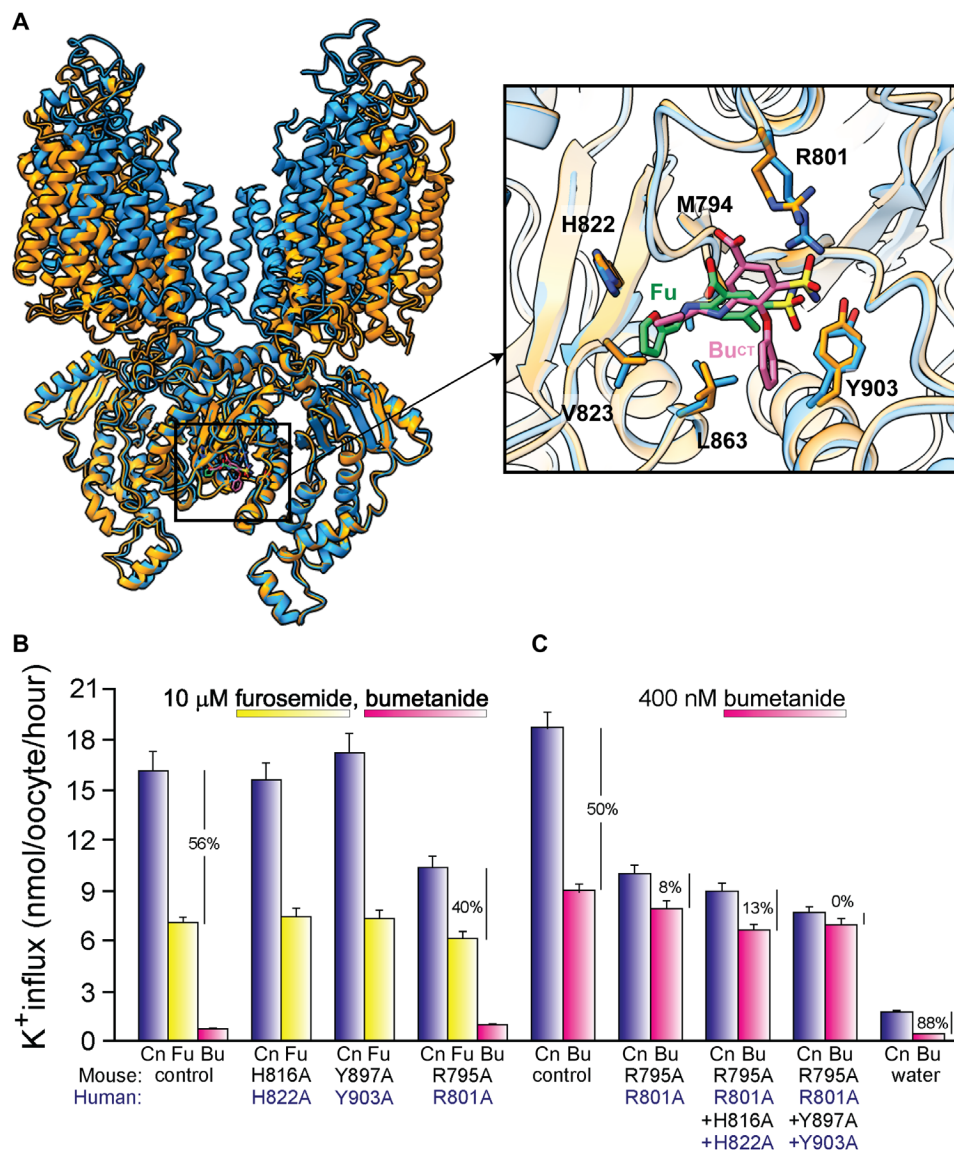
Fig. 5. Effect of Fu and/or Bu on wild-type and mutant mNKCC1 cotransporters. (**A**) The Fu/Bu binding site based on the hNKCC1-Fu-I and hNKCC1-Bu cryo-EM structures. The dimers of hNKCC1-Fu-I and hNKCC1-Bu are colored cyan and orange, respectively. The bound Fu (in hNKCC1-Fu-I) and Bu_{CT} (in hNKCC1-Bu) molecules are represented by green and pink sticks. Residues involved in Fu/Bu binding are in stick models (cyan for Fu binding; orange for Bu_{CT} binding). (**B**) K^+ influx measurements in *X. laevis* oocytes injected with cRNA encoding wild-type or mutant NKCC1 cRNA. Fluxes were measured in the presence of ouabain (200 µM) and the presence or absence of 10 µM Fu or Bu. The mutant cotransporters were of amino acids identified by cryo-EM as CTD residues participating in binding of inhibitors. (**C**) K^+ influx measurements in oocytes injected with wild-type or mutant transporter cRNA and, in this case, subjected to Bu at its ~EC_{50} concentration, i.e., 400 nM. Fluxes are expressed in nanomoles K^+ per oocyte per hour. Bars represent means ± SEM (20 to 25 oocytes).

TM region (*29*). It has been previously reported that the CTD of dimeric NKCC1 can be reversibly split to participate in its regulation and activation (*30*). Therefore, the transport mechanism of this cotransporter may be involved in reversibly switching of the oligomerization states of both the TMD and CTD. The change in conformation of hNKCC1 triggered by the binding of Fu and Bu is summarized in fig. S14.

The splitting of the hNKCC1 dimer at the TMD can be easily explained on the basis of the cryo-EM structures of hNKCC1. The structures indicate that TM11 and TM12 of each subunit are responsible for forming the dimer interface at the TMD. These two TM

helices are significantly shorter (about 50%) when compared with the other TM helices, significantly decreasing the area of subunit-subunit interface at the TMD within the hNKCC1 dimer. Therefore, it is not unexpected that the TMD of hNKCC1 can readily shift its oligomerization state from dimeric to monomeric. Further experiments are needed to understand the relationship between the different oligomerization states of the TMD and the function of this cotransporter.

Our structural and mutagenesis data suggest that the hNKCC1 cotransporter has two inhibitor-binding sites. First, our study indicates that the CTD of hNKCC1 forms an inhibitor-binding site (Fu and Bu_{CT} sites). It is observed that the locations of bound Fu and

Bu_{CT} overlap with each other, where hNKCC1 uses the same set of amino acids to anchor these two inhibitors. It appears that these binding residues are important for the sensitivity of the cotransporter to these inhibitors as seen in our mutagenesis experiments. Unexpectedly, the TMD of hNKCC1 also forms an additional inhibitor-binding site (Bu_{TM} site). The cavity located between TMs 1, 3, 6, 8, 9, and 10 and near the extracellular surface of the hNKCC1 protomer creates one of the inhibitor-binding sites. The observation of this site is in good agreement with previous mutagenesis data that suggested that the inhibitors bind within the TMD (28). While this manuscript was under review, Zhao *et al.* (31) reported a structure of hNKCC1 bound by Bu, where Bu was found in the TMD and Bu binding also triggered a separation between the two hNKCC1 protomers at the TMD, thereby agreeing with our structural findings.

Our observation is consistent with the demonstration of large movements of C terminus associated with activation of the cotransporter (30). Note that our work poses a possibility that the two inhibitor-binding sites may couple with each other. The long-distance conformational coupling and movement between the CTD and TMD of this transporter may result in inhibiting the transport of ions across the membrane. Long-distance conformational couplings are not unusual for these cotransporters. For example, TM2 is located approximately 12 Å from the K^+ ion and even further (18 Å) from the predicted Na^+ ion. Therefore, no residues from this TM helix directly coordinate ion binding. In NKCC2, TM2 is encoded by exon 5, an alternatively spliced cassette exon that comes in three flavors (A, B, and F) (32, 33). Along the kidney nephron, NKCC2-B is expressed in the cortex where the Na^+ concentration is low, and consequently, the transporter has a high affinity for Na^+. NKCC2-F, which is expressed deeper in the medulla where the Na^+ is high, has a much lower affinity for Na^+. These distinct Na^+ affinities, encoded within TM2, can only be explained by long-distance conformational couplings. Nonetheless, exactly how these two inhibitor-binding sites couple together via a long distance must await further investigation.

MATERIALS AND METHODS
Expression and purification of hNKCC1
The codon-optimized DNA of full-length hNKCC1 was synthesized and cloned into pcDNA3.1-FLAG (GenScript) in frame with a thrombin cleavage site and FLAG tag at the N terminus. The resulting plasmid was confirmed by the Sanger method of DNA sequencing. Human embryonic kidney Expi293F (Thermo Fisher Scientific) cells were cultured in Expi293 Expression Medium (Gibco) at 37°C supplemented with 8% CO_2. The NKCC1 protein was expressed using a transient expression system with the following procedures. The purified pcDNA3.1-FLAG plasmid expressing full-length hNKCC1 was mixed with cationic liposomes (transfection reagent I, Avanti Polar Lipid) at a 1:10 (DNA: liposome; w/w) ratio in Opti-MEM I reduced-serum medium (Gibco) and incubated at room temperature for 20 min. The resulting plasmid/liposome complex was added to cells (cell density of 2.5×10^6 to 3×10^6 cells/ml) at a final DNA concentration of 1 mg/liter. To boost protein expression, valproic acid (Sigma-Aldrich) was added after 18 to 24 hours to a final concentration of 3 mM. The cells were incubated for a total of 72 hours, collected, resuspended in buffer A [20 mM Hepes-NaOH (pH 7.5) and 20 mM NaCl], and disrupted with a French pressure cell. The membrane fraction was collected and washed once with buffer A. The membrane protein was then solubilized in 1% (w/v) glycol-diosgenin (GDN; Anatrace) for 3 hours at 4°C. Insoluble material was removed by ultracentrifugation at 40,000g. The supernatant was applied to anti-FLAG M2 affinity gel (MilliporeSigma) and washed with buffer B (buffer A with protease inhibitors and 0.01% GDN; Anatrace); then, the protein was eluted by FLAG peptide (0.2 mg/ml). Last, the protein was concentrated using a 100-kDa cutoff centrifugal filter (Millipore) and further purified using size exclusion chromatography (Superose 6, 10/300, GE Healthcare) in buffer B. The peak fractions were confirmed through SDS–polyacrylamide gel electrophoresis analysis and concentrated for cryo-EM sample preparation.

EM sample preparation
The hNKCC1 samples were concentrated to 5 mg/ml. The samples were then double-blotted onto glow-discharged holey carbon grids (Quantifoil Cu R1.2/1.3; 300 mesh). The initial blot contained 1 μl of sample blotted for 2.5 s at 5 force, followed by a second 2 μl blot for 10 s at 10 force, and then plunge-frozen in liquid ethane using a Vitrobot (Thermo Fisher Scientific). The grids were transferred into cartridges. For high-resolution data collection, the sample grids were loaded into a Titan Krios cryo-EM operated at 300 kV equipped with Gatan BioQuantum imaging filter and a K3 summit direct electron detector (Gatan). The micrographs were recorded using SerialEM (34) multishot method over nine neighboring holes (3 × 3) with counting mode at nominal ×81,000 magnification corresponding to a calibrated pixel size of 1.07 Å (superresolution, 0.535 Å per pixel) and a defocus range of −1 to −2.5 μm. To remove inelastically scattered electrons, the slit width was set to 20 eV. Each micrograph was exposed for 3.0 s with a total specimen dose of 41.0 e^-/A^2, and 60 frames were captured per specimen area. For the hNKCC1 inhibitor complexes, either Fu (100 μM) or Bu (100 μM) was added to the sample and incubated for 2 hours to form the complex. The procedures for making cryo-EM grids and high-resolution cryo-EM data collection were the same as those of apo-hNKCC1. Each micrograph was exposed for 4.0 s with a total specimen dose of 41.0 e^-/A^2, and 40 frames were captured per specimen area.

Cryo-EM data acquisition
The micrographs of hNKCC1 were aligned by using patch-based motion correction for beam-induced motion using cryoSPARC (35). The contrast transfer function (CTF) parameters of the micrographs were determined using patch CTF (36). After manual inspection and sorting to discard poor micrographs, ~2000 particles of hNKCC1 were manually picked to generate templates for automatic picking. Initially, 6,250,321 particles were selected after autopicking in cryoSPARC (35).

From picked particle sets, particles were classified and final maps were solved with the use of the BaR methodology (figs. S1 to S3) (24). Briefly, for build phase, several iterative rounds of 2D classifications were carried to remove false picks and classes with unclear features. The resulting particles were used to generate four to five reference free ab initio 3D reconstructions with C1 symmetry. These initial classes were used to retrieve particles from picked particle stack. 3D classifications using maps determined from the build phase of BaR were applied to the particle sets. The new particle subset shows that clear features were further cleaned using multiple rounds of 2D classifications and 3D classifications.

The resulting 244,106 particles were chosen for further processing with nonuniform and local CTF refinement (36). The local focused refinement with a soft mask covering the hNKCC1 protein area was

done using cryoSPARC (*35*), resulting in a 3.47 Å global resolution map based on the gold-standard Fourier shell correlation (FSC 0.143).

For the hNKCC1-Fu sample, 2,144,822 particles were initially selected from autopicking in cryoSPARC (*35*). After several rounds of 2D classifications, 549,545 particles were selected to generate ab initio reconstructions for processing using the BaR methodology as previously described (*24*). After four cycles of 3D classification, the resulting 156,711 particles of hNKCC1-Fu-I and 147,729 particles of hNKCC1-Fu-II were selected for further processing with nonuniform and local CTF refinement (*36*). A soft mask covering the hNKCC1 protein area was used for the final local focused refinement, resulting in a 3.33 Å global resolution map for hNKCC1-Fu-I based on the gold-standard Fourier shell correlation (FSC 0.143). The hNKCC1-Fu-II dimer resulted in a focused resolution map at 3.87 Å based on the gold-standard Fourier shell correlation (FSC 0.143).

For the hNKCC1-Bu sample, 9,858,365 particles were initially selected from autopicking in cryoSPARC (*35*). After several rounds of 2D classifications, 437,493 particles were then used to generate ab initio reconstructions and processed using the BaR methodology as previously described (*24*). After four cycles of 3D classification, the resulting 53,597 particles of hNKCC1-Bu were selected for further processing with nonuniform refinement (*36*). A soft mask covering the hNKCC1 protein area was used for the final local focused refinement, resulting in a 3.28 Å global resolution map for hNKCC1-Bu based on the gold-standard Fourier shell correlation (FSC 0.143).

Model building and structure refinement

Model building of apo-hNKCC1 was based on the 3.47 Å cryo-EM map. The homology modeling structure of hNKCC1 generated by the SWISS-MODEL server (*37*) based on the atomic coordinates of the NKCC1 transporter from *D. rerio* [Protein Data Bank (PDB) ID: 6NPL] (*19*) was used as the initial model with Chimera (*38*). The subsequent model rebuilding was performed using Coot (*39*). Structure refinements were performed using the phenix.real_space_refine program (*40*) from the PHENIX suite (*41*). The final atomic model was evaluated using MolProbity (*42*). The statistics associated with data collection, 3D reconstruction, and model refinement are included in table S1.

Model building of hNKCC1-Fu-I, hNKCC1-Fu-II, and hNKCC1-Bu were based on their corresponding cryo-EM maps with resolutions of 3.33, 3.87, and 3.28 Å, respectively. The initial models for these structures were based on the apo-hNKCC1 structure. Subsequent model buildings and refinements were the same as those for apo-hNKCC1. The statistics of these structures associated with data collection, 3D reconstruction, and model refinement are included in table S1.

Site-directed mutagenesis and complementary RNA transcription

Small fragments of mouse NKCC1 (mNKCC1) cDNA subcloned into pBSK was subjected to mutagenesis using the QuikChange site-directed mutagenesis kit (Agilent, Santa Clara, CA). Complementary oligonucleotides containing desired mutation were used to start the DNA synthesis. Parental vector methylated in bacteria was digested with Dpn I leaving the synthetized DNA to be transfected into bacteria. Mutations and the integrity of the rest of the sequences were verified by Sanger sequencing, with the small fragments reinserted into the full-length mNKCC1 clone in the oocyte expressing vector, pBF. The final clones were sequenced to ensure the presence of the mutation, linearized with Mlu I at the 3′ end and transcribed into complementary RNA (cRNA) using the mMESSAGE mMACHINE SP6 transcription kit (Ambion, through Thermo Fisher Scientific). After deoxyribonuclease treatment, the RNA was precipitated with LiCl; washed with 75% ethanol; resuspended in nuclease-free water; and quantified by measuring the optical density at 260, 280, and 320 nm.

X. laevis oocyte isolation and injection

Oocyte-positive *X. laevis* oocytes were maintained in a static environment as previously described (*43*). Under tricaine anesthesia, a small lateral incision in the abdomen was made, and ovary lobes containing oocytes were excised. After suturing the abdomen with three monofilament nylon stiches, lobes were minced into smaller pieces, incubated in Ca^{2+}-free, 180-mosM, saline containing collagenase (10 mg/ml; 4×5 ml, 90 min each) at 4°C in a 50-ml conical tube on a shaker. Then, under a dissecting microscope, oocytes were singly isolated and placed in 35-mm dishes in L15 medium [250 ml of Leibovitz saline from Invitrogen + 200 ml of water + 954 mg of Hepes (pH 7.4); osmolarity, 200 mosM] supplemented with gentamycin (8 mg/ml) and kept at 16°C. Following the day of injection, oocytes were injected with 50 nl of water containing 15 ng of transporter cRNA. Oocytes were returned to the 16°C incubator, and L15 medium was replaced daily until flux experiment.

K+ influx measurements

Activity of the mNKCC1 cotransporter was determined 3 days after injection. Groups of 20 to 25 oocytes placed in 35-mm dishes were rinsed with 3 ml of isosmotic saline [96 mM NaCl, 4 mM KCl, 2 mM CaCl₂, 1 mM MgSO₄, 5 mM Hepes (pH 7.4), and 200 mosM]. The solution was aspirated and replaced with 1 ml of identical solution containing 200 mM ouabain for a 10-min preincubation period. At the end of the preincubation, the solution was aspirated and replaced with hyperosmotic solution containing 200 μM ouabain and ^{83}Rb (2.5 μCi/ml) and with or without 400 nM or 10 μM Bu or 10 μM Fu. Two aliquots of 5 nl were sampled from the solution bathing the oocytes to serve as standards. The uptake was stopped 60 min later by aspiration of the uptake solution and four rapid washes with ice-cold hyperosmotic solution. Oocytes were pipetted into individual scintillation vials, lysed into 200 ml of 0.5 M NaOH for 1 hour, and neutralized with 100 ml of glacial acetic acid. Bio-Safe II scintillation liquid (5 ml) was added to each vial, and counts were transformed into pmoles K+. Influx is expressed in pmoles K+ per oocyte per hour.

MD simulations

The protonation states of the titratable residues of the hNKCC1 transporter were determined using the H++ server (http://biophysics.cs.vt.edu/). The apo-hNKCC1 structure was immersed in an explicit lipid bilayer of 1-palmitoyl-2-oleoyl-sn-glycero-3-phosphocholine (POPC) and 1-palmitoyl-2-oleoyl-sn-glycero-3-phosphoethanolamine (POPE) with molecular ratio of 1:1 and a water box with dimensions of 148.9 Å by 148.9 Å by 193.1 Å using the CHARMM-GUI Membrane Builder webserver (www.charmm-gui.org/?doc=input/membrane). NaCl (75 mM), KCl (75 mM) and extra neutralizing counter ions were added into the system. The total atoms of the system were 322,981. The tleap program was used to generate parameter and coordinate files using ff14SB and Lipid17 force field for protein and lipids, respectively. The PMEMD.CUDA program in AMBER18 (AMBER 2018, University of California San Francisco) was used to conduct the MD simulations. The MD simulations were performed with periodic

boundary conditions to produce isothermal-isobaric ensembles. An external voltage (0.06 V/nm) was added to the systems from the extracellular to the intracellular side (*44–46*). Long-range electrostatics was calculated using the particle mesh Ewald method (*47*) with a 10 Å cutoff. Before the production runs, energy minimization was carried out to optimize the system. Subsequently, the system was heated from 0 to 303 K using Langevin dynamics with the collision frequency of 1 ps^{-1}. During heating, the hNKCC1 transporter was position-restrained using an initial constant force of 500 kcal/mol/$Å^2$ and weakened to 10 kcal/mol/$Å^2$, allowing lipid and water molecules to move freely. The system was then going through 5-ns equilibrium MD simulations. Last, a total of 1-μs production MD simulations was conducted, and coordinates were saved every 100 ps for analysis. The system was well equilibrated after 100-ns simulations according to RMSDs of the transporter Cα atoms. A 100- to 1000-ns trajectory of the system was used for RMSF and PCA analysis (*48, 49*). GROMCAS analysis tools were used for the MD simulation trajectory analysis (*50*).

SUPPLEMENTARY MATERIALS
Supplementary material for this article is available at https://science.org/doi/10.1126/sciadv.abq0952

REFERENCES AND NOTES
1. M. Haas, The Na-K-Cl cotransporters. *Am. J. Physiol. Cell Physiol.* **267**, C869–C885 (1994).
2. S. C. Hebert, D. B. Mount, G. Gamba, Molecular physiology of cation-coupled Cl- cotransport: The SLC12 family. *Pflugers Arch.* **447**, 580–593 (2004).
3. G. Gamba, Molecular physiology and pathophysiology of electroneutral cation-chloride cotransporters. *Physiol. Rev.* **85**, 423–493 (2005).
4. E. Delpire, K. B. Gagnon, Na^+ -K^+ -$2Cl^-$ cotransporter (NKCC) physiological function in nonpolarized cells and transporting epithelia. *Compr. Physiol.* **8**, 871–901 (2018).
5. E. Delpire, L. Wolfe, B. Flores, R. Koumangoye, C. C. Schornak, S. Omer, B. Pusey, C. Lau, T. Markello, D. R. Adams, A patient with multisystem dysfunction carries a truncation mutation in human *SLC12A2*, the gene encoding the Na-K-2Cl cotransporter, NKCC1. *Cold Spring Harb. Mol. Case Stud.* **2**, a001289 (2016).
6. E. F. Macnamara, A. E. Koehler, P. D'Souza, T. Estwick, P. Lee, G. Vezina; Undiagnosed Diseases Network, H. Fauni, S. R. Braddock, E. Torti, J. M. Holt, P. Sharma, M. C. V. Malicdan, C. J. Tifft, Kilquist syndrome: A novel syndromic hearing loss disorder caused by homozygous deletion of SLC12A2. *Hum Mutat.* **40**, 532–538 (2019).
7. H. Mutai, K. Wasano, Y. Momozawa, Y. Kamatani, F. Miya, S. Masuda, N. Morimoto, K. Nara, S. Takahashi, T. Tsunoda, K. Homma, M. Kubo, T. Matsunaga, Variants encoding a restricted carboxy-terminal domain of SLC12A2 cause hereditary hearing loss in humans. *PLOS Genet.* **16**, e1008643 (2020).
8. T. Stödberg, M. Magnusson, N. Lesko, A. Wredenberg, D. Martin Munoz, H. Stranneheim, A. Wedell, *SLC12A2* mutations cause NKCC1 deficiency with encephalopathy and impaired secretory epithelia. *Neurol Genet.* **6**, e478 (2020).
9. R. Koumangoye, L. Bastarache, E. Delpire, NKCC1: Newly found as a human disease-causing ion transporter. *Function* **2**, zqaa028 (2021).
10. A. McNeill, E. Iovino, L. Mansard, C. Vache, D. Baux, E. Bedoukian, H. Cox, J. Dean, D. Goudie, A. Kumar, R. Newbury-Ecob, C. Fallerini, A. Renieri, D. Lopergolo, F. Mari, C. Blanchet, M. Willems, A.-F. Roux, T. Pippucci, E. Delpire, SLC12A2 variants cause a neurodevelopmental disorder or cochleovestibular defect. *Brain* **143**, 2380–2387 (2020).
11. I. E. McCoy, G. M. Chertow, T. I.-H. Chang, Patterns of diuretic use in the intensive care unit. *PLOS ONE* **14**, e0217911 (2019).
12. E. Delpire, J. M. Lu, R. England, C. Dull, T. Thorne, Deafness and imbalance associated with inactivation of the secretory Na-K-2Cl co-transporter. *Nat. Genet.* **22**, 192–195 (1999).
13. P. Hannaert, M. Alvarez-Guerra, D. Pirot, C. Nazaret, R. P. Garay, Rat NKCC2/NKCC1 cotransporter selectivity for loop diuretic drugs. *Naunyn Schmiedebergs Arch. Pharmacol.* **365**, 193–199 (2002).
14. E. J. Kim, M. G. Lee, Pharmacokinetics and pharmacodynamics of intravenous bumetanide in mutant Nagase analbuminemic rats: Importance of globulin binding for the pharmacodynamic effects. *Biopharm. Drug Dispos.* **22**, 147–156 (2001).
15. P. C. Walker, N. S. Berry, D. J. Edwards, Protein binding characteristics of bumetanide. *Dev. Pharmacol. Ther.* **12**, 13–18 (1989).
16. T. Wang, L. Shan, M. Miao, Z. Xu, F. Jia, Treatment effect of bumetanide in children with autism spectrum disorder: A systematic review and meta-analysis. *Front. Psych.* **12**, 751575 (2021).
17. E. Lemonnier, N. Villeneuve, S. Sonie, S. Serret, A. Rosier, M. Roue, P. Brosset, M. Viellard, D. Bernoux, S. Rondeau, S. Thummler, D. Ravel, Y. Ben-Ari, Effects of bumetanide

18. on neurobehavioral function in children and adolescents with autism spectrum disorders. *Transl. Psychiatry* **7**, e1056 (2017).
18. E. Lemonnier, G. Robin, C. Degrez, R. Tyzio, M. Grandgeorge, Y. Ben-Ari, Treating Fragile X syndrome with the diuretic bumetanide: A case report. *Acta Paediatr.* **102**, e288–e290 (2013).
19. T. A. Chew, B. J. Orlando, J. R. Zhang, N. R. Latorraca, A. Wang, S. A. Hollingsworth, D. H. Chen, R. O. Dror, M. F. Liao, L. Feng, Structure and mechanism of the cation–chloride cotransporter NKCC1. *Nature* **572**, 488–492 (2019).
20. P. Janoš, A. Magistrato, All-atom simulations uncover the molecular terms of the NKCC1 transport mechanism. *J. Chem. Inf. Model.* **61**, 3649–3658 (2021).
21. X. Y. Yang, Q. Z. Wang, E. H. Cao, Structure of the human cation-chloride cotransporter NKCC1 determined by single-particle electron cryo-microscopy. *Nat. Commun.* **11**, 11 (2020).
22. S. Liu, S. Chang, B. Han, L. Xu, M. Zhang, C. Zhao, W. Yang, F. Wang, J. Li, E. Delpire, S. Ye, X.-C. Bai, J. Guo, Cryo-EM structures of the human cation-chloride cotransporter KCC1. *Science* **366**, 505–508 (2019).
23. Y. Xie, S. Chang, C. Zhao, F. Wang, S. Liu, J. Wang, E. Delpire, S. Ye, J. Guo, Structures and an activation mechanism of human potassium-chloride cotransporters. *Sci. Adv.* **6**, eabc5883 (2020).
24. C.-C. Su, M. Lyu, C. E. Morgan, J. R. Bolla, C. V. Robinson, E. W. Yu, A "Build and Retrieve" methodology to simultaneously solve cryo-EM structures of membrane proteins. *Nat. Methods* **18**, 69–75 (2021).
25. P. Isenring, B. Forbush, Ion and bumetanide binding by the Na-K-Cl Cotransporter. *J. Biol. Chem.* **272**, 24556–24562 (1997).
26. P. Isenring, S. Jacoby, J.-T. Chang, B. Forbush, Mutagenic mapping of the Na-K-Cl cotransporter for domains involved in ion transport and bumetanide binding. *J. Gen. Physiol.* **112**, 549–558 (1998).
27. P. Isenring, S. C. Jacoby, B. Forbush, The role of transmembrane domain 2 in cation transport by the Na-K-Cl cotransporter. *Proc. Natl. Acad. Sci. U.S.A.* **95**, 7179–7184 (1998).
28. S. Somasekharan, J. Tanis, B. Forbush, Loop diuretic and ion-binding residues revealed by scanning mutagenesis of transmembrane helix 3 (TM3) of Na-K-Cl cotransporter (NKCC1) *. *J. Biol. Chem.* **287**, 17308–17317 (2012).
29. C. E. Morgan, P. Glaza, I. V. Leus, A. Trinh, C.-C. Su, M. Cui, H. I. Zgurskaya, E. W. Yu, Cryoelectron microscopy structures of AdeB illuminate mechanisms of simultaneous binding and exporting of substrates. *mBio* **12**, e03690-20 (2021).
30. M. Y. Monette, B. Forbush, Regulatory activation is accompanied by movement in the C terminus of the Na-K-Cl cotransporter (NKCC1). *J. Biol. Chem.* **287**, 2210–2220 (2012).
31. Y. Zhao, K. Roy, P. Vidossich, L. Cancedda, M. De Vivo, B. Forbush, E. Cao, Structural basis for inhibition of the cation-chloride cotransporter NKCC1 by the diuretic drug bumetanide. *Nat. Commun.* **13**, 2747 (2022).
32. C. Plata, P. Meade, N. Vazquez, S. C. Hebert, G. Gamba, Functional properties of the apical Na+-K+-2Cl- cotransporter isoforms. *J. Biol. Chem.* **277**, 11004–11012 (2002).
33. I. Giménez, P. Isenring, B. Forbush, Spatially distributed alternative splice variants of the renal Na-K-Cl cotransporter exhibit dramatically different affinities for the transported ions. *J. Biol. Chem.* **277**, 8767–8770 (2002).
34. D. N. Mastronarde, SerialEM: A program for automated tilt series acquisition on tecnai microscopes using prediction of specimen position. *Microsc. Microanal.* **9**, 1182–1183 (2003).
35. A. Punjani, J. L. Rubinstein, D. J. Fleet, M. A. Brubaker, cryoSPARC: Algorithms for rapid unsupervised cryo-EM structure determination. *Nat Methods.* **14**, 290–296 (2017).
36. K. Zhang, Gctf: Real-time CTF determination and correction. *J. Struct. Biol.* **193**, 1–12 (2016).
37. A. Waterhouse, M. Bertoni, S. Bienert, G. Studer, G. Tauriello, R. Gumienny, F. T. Heer, T. A. P. de Beer, C. Rempfer, L. Bordoli, R. Lepore, T. Schwede, SWISS-MODEL: Homology modelling of protein structures and complexes. *Nucleic Acids Res.* **46**, W296–W303 (2018).
38. E. F. Pettersen, T. D. Goddard, C. C. Huang, G. S. Couch, D. M. Greenblatt, E. C. Meng, T. E. Ferrin, UCSF Chimera—A visualization system for exploratory research and analysis. *J. Comput. Chem.* **25**, 1605–1612 (2004).
39. P. Emsley, K. Cowtan, Coot: Model-building tools for molecular graphics. *Acta Crystallogr. D Biol. Crystallogr.* **60**, 2126–2132 (2004).
40. P. V. Afonine, B. K. Poon, R. J. Read, O. V. Sobolev, T. C. Terwilliger, A. Urzhumtsev, P. D. Adams, Real-space refinement in PHENIX for cryo-EM and crystallography. *Acta Crystallogr. D Struct. Biol.* **74**, 531–544 (2018).
41. P. D. Adams, R. W. Grosse-Kunstleve, L. W. Hung, T. R. Ioerger, A. J. McCoy, N. W. Moriarty, R. J. Read, J. C. Sacchettini, N. K. Sauter, T. C. Terwilliger, PHENIX: Building new software for automated crystallographic structure determination. *Acta Crystallogr. D Biol. Crystallogr.* **58**, 1948–1954 (2002).
42. V. B. Chen, W. B. Arendall III, J. J. Headd, D. A. Keedy, R. M. Immormino, G. J. Kapral, L. W. Murray, J. S. Richardson, D. C. Richardson, MolProbity: All-atom structure validation for macromolecular crystallography. *Acta Crystallogr. D Biol. Crystallogr.* **66**, 12–21 (2010).
43. E. Delpire, K. B. Gagnon, J. J. Ledford, J. M. Wallace, Housing and husbandry of Xenopus laevis affect the quality of oocytes for heterologous expression studies. *J. Am. Assoc. Lab. Anim. Sci.* **50**, 46–53 (2011).

44. D. L. Li, T. H. Jin, D. Gazgalis, M. Cui, D. E. Logothetis, On the mechanism of GIRK2 channel gating by phosphatidylinositol bisphosphate, sodium, and the Gβγ dimer. *J. Biol. Chem.* **294**, 18934–18948 (2019).

45. X. Y. Meng, H. X. Zhang, D. E. Logothetis, M. Cui, The molecular mechanism by which PIP$_2$ opens the intracellular G-loop gate of a Kir3.1 channel. *Biophys. J.* **102**, 2049–2059 (2012).

46. X. Y. Meng, S. T. Liu, M. Cui, R. H. Zhou, D. E. Logothetis, The molecular mechanism of opening the helix bundle crossing (HBC) Gate of a Kir channel. *Sci. Rep.* **6**, 29399 (2016).

47. T. Darden, D. York, L. Pedersen, Particle mesh Ewald: An N·log(N) method for Ewald sums in large systems. *J. Chem. Phys.* **98**, 10089–10092 (1993).

48. A. Amadei, A. B. Linssen, H. J. Berendsen, Essential dynamics of proteins. *Proteins* **17**, 412–425 (1993).

49. A. Amadei, M. A. Ceruso, A. Di Nola, On the convergence of the conformational coordinates basis set obtained by the essential dynamics analysis of proteins' molecular dynamics simulations. *Proteins* **36**, 419–424 (1999).

50. H. Bekker, H. Berendsen, E. Dijkstra, S. Achterop, R. Vondrumen, D. Vanderspoel, A. Sijbers, H. Keegstra, M. Renardus, GROMACS–A parallel computer for molecular-dynamics simulations, in *Proceedings of the 4th International Conference on Computational Physics (PC 92)* (SAO/NASA Astrophysics Data System, 1993), pp. 252–256.